Geophysical Research Letters

RESEARCH LETTER

10.1029/2025GL119309

Key Points:

- We present SS3DPacific: a new VSV model of the Pacific ocean with 3D resolution and uncertainty
- We show that interpretations of oceanic lithosphere cooling are strongly biased by vertical resolution smearing
- An anomalous band-pattern aligned with fracture zones points to lateral complexities in the cooling of the oceanic lithosphere

Supporting Information:

Supporting Information may be found in the online version of this article.

Correspondence to:

P. Koelemeijer,
paula.koelemeijer@earth.ox.ac.uk

Citation:

Latallerie, F., Koelemeijer, P., Walker, A., Maggi, A., Lambotte, S., & Zaroli, C. (2026). New insights into the cooling of the oceanic lithosphere from surface-wave tomographic inferences. *Geophysical Research Letters*, *53*, e2025GL119309. https://doi.org/10.1029/2025GL119309

Received 9 OCT 2025
Accepted 3 FEB 2026

Author Contributions:

Conceptualization: Franck Latallerie, Paula Koelemeijer, Andrew Walker, Alessia Maggi, Sophie Lambotte, Christophe Zaroli
Data curation: Franck Latallerie
Formal analysis: Franck Latallerie, Paula Koelemeijer, Andrew Walker
Funding acquisition: Paula Koelemeijer, Andrew Walker
Investigation: Franck Latallerie, Paula Koelemeijer, Andrew Walker, Christophe Zaroli
Methodology: Franck Latallerie, Paula Koelemeijer, Andrew Walker, Christophe Zaroli
Project administration: Paula Koelemeijer, Andrew Walker

New Insights Into the Cooling of the Oceanic Lithosphere From Surface-Wave Tomographic Inferences

Franck Latallerie[1], Paula Koelemeijer[1], Andrew Walker[1], Alessia Maggi[2], Sophie Lambotte[2], and Christophe Zaroli[2]

[1]Department of Earth Sciences, University of Oxford, Oxford, UK, [2]Institut Terre et Environement de Strasbourg, UMR7063, Université de Strasbourg, EOST/CNRS, Strasbourg, France

Abstract How oceanic plates cool and thicken with age remains a subject to debate, with several thermal models supported by apparently contradictory data. Combining a novel imaging technique that balances resolution and uncertainty with finite-frequency surface-wave measurements, we build tomographic model SS3DPacific to revisit the cooling style of the oceanic lithosphere beneath the Pacific ocean. Resolution analysis indicates a strong vertical smearing that biases estimates of the apparent lithospheric thickness, limiting the ability to discriminate between the half space and plate cooling models. Laterally, a pattern of anomalous bands in seismic velocity aligned with fracture zones points to additional lateral complexities in the lithosphere, complicating simple age-trend analyses.

Plain Language Summary As the seafloor spreads away from mid-oceanic ridges, material cools down and the lithosphere, often defined by a temperature boundary, thickens. However, exactly how the lithosphere cools with age remains subject of debate. Some models suggest that it continues to cool down and thicken, others propose that the lower boundary of the lithosphere flattens due to secondary processes. Here, we investigate this problem using seismic imaging of the oceanic lithosphere. Our novel method allows us to assess quantitatively whether imaged structures are real or imaging artifacts. We show that imaging limitations do not allow us to discriminate between two widely used models of the cooling of the oceanic lithosphere. Our results also show anomalous bands that line up with fractures in the oceanic crust. These point to lateral complexities in the cooling style of the oceanic lithosphere.

1. Introduction

Plate tectonics describes the motions of plates over the Earth's surface, with oceanic lithosphere being created at mid-oceanic ridges and sinking into the mantle in subduction zones. As oceanic plates move away from the ridges, they cool down by heat diffusion, thicken, and subside as evident in global bathymetry, heat flow, and gravity observations (Richards et al., 2020; Richardson et al., 1995). However, our understanding of the structure and evolution of oceanic plates remains simplified and subject of debate. Two heat diffusion models are often adopted for describing the thermal structure of the oceanic lithosphere: the Half-Space-Cooling (HSC) and Plate-Cooling (PC) models. HSC simply considers the lithosphere as an infinite half space cooling with age. While attractive for its simplicity, it does not match the apparent flattening of the lithosphere thickness at older ages supported by heat flow and bathymetry data. PC includes a boundary condition at depth that produces the apparent flattening (McKenzie, 1967; Parsons & Sclater, 1977). However, this ad hoc constraint assumes the existence of underlying physical processes that remain to be clarified (e.g., small-scale sub-lithospheric convection cells, Ballmer et al., 2009). Proponents of the HSC model reconcile it with observations either by adding complexity, such as secular cooling (e.g., Korenaga et al., 2021), or by calling attention to the inherent limitations of heat flow or bathymetry measurements (e.g., the effect of sediment layers, Richards et al., 2020) or uncertainty and resolution artifacts in seismic imaging (e.g., Rawlinson et al., 2014). New observations, with better uncertainty quantification, are required to address this problem.

Beyond the simple diffusive cooling of the lithosphere, bathymetry data show that oceanic plates are not smooth plates, but include great intraplate complexity (Figure 1), such as linear hotspot tracks, sea mounts and fracture zones. The effect of these structures on the thermal structure of the lithosphere remains unclear, and is at present poorly accounted for in studies of the cooling of the lithosphere (Matthews et al., 2011; Wessel & Haxby, 1990).

Software: Franck Latallerie, Sophie Lambotte, Christophe Zaroli
Supervision: Paula Koelemeijer, Andrew Walker
Visualization: Franck Latallerie
Writing – original draft: Franck Latallerie, Paula Koelemeijer, Andrew Walker
Writing – review & editing: Franck Latallerie, Paula Koelemeijer, Andrew Walker, Alessia Maggi, Christophe Zaroli

Bathymetry, heat flow, gravity, seismic refraction and reflection data all provide crucial information for studying the oceanic lithosphere. However, constraints are either local or depth integrated and they are often strongly influenced by shallow Earth structure (e.g., crust and sediment cover). Surface-wave tomography is a complementary technique: surface waves are sensitive to temperature and offer global or basin-scale constraints (Auer et al., 2014; French et al., 2013; Isse et al., 2019; Maggi et al., 2006; Ritzwoller et al., 2004; Zhou et al., 2006). However, surface-wave data are contaminated by noise and theoretical errors, while seismic imaging is hindered by the heterogeneous source-receiver distribution and convoluted depth sensitivities. As a consequence, model resolution and uncertainty is often complex, but crucial to assess for robust interpretations (Freissler et al., 2024; Latallerie et al., 2022; Rawlinson et al., 2014; Ritsema et al., 2007). In practice, resolution and uncertainty are difficult to control, and computationally expensive to obtain for large-scale imaging problems (An, 2012; Fichtner & Trampert, 2011; Nolet et al., 1999; Ritsema & Lekić, 2020).

Here, we provide new constraints on the oceanic lithosphere using the 3D imaging framework of Latallerie, Zaroli, et al. (2025). This approach combines the power of finite-frequency theory for surface waves (Snieder, 1986; Zhou, 2009a) with the Backus-Gilbert based SOLA method (Backus & Gilbert, 1968; Pijpers & Thompson, 1994; Zaroli, 2016) for inferring Earth structure. Finite-frequency offers a more accurate and fully three-dimensional one-step framework, while SOLA provides control on resolution and uncertainty, also making these readily available by construction. Using this approach, we develop SS3DPacific, a new 3D model of the vertically polarized shear-wave velocity (V_{SV}) for the Pacific uppermost mantle. Equipped with SS3DPacific, its 3D resolution and uncertainty, we revisit the age cooling trend of the lithosphere, and discuss our ability to discriminate between the HSC and PC models. Beyond the simple age dependence of lithospheric cooling, we also discuss further complexities in the structure of the lithosphere.

2. Data and Method

We measure surface-wave phase-delays relative to 1D model STW105 (Kustowski et al., 2008) between 6 and 21 mHz adopting the approach of Latallerie, Zaroli, et al. (2025). To obtain measurement uncertainty estimates, we use a multi-taper technique. We select high-quality data based on a set of criteria, including spatial homogeneisation, resulting in a subset of 44,917 measurements (Figures 2a and 2b). The crustal signature is removed from the data using crustal model CRUST1.0 (Bassin et al., 2000).

We combine 3D finite-frequency theory and SOLA inferences, relating fundamental-mode Rayleigh-wave phase-delays measured on the vertical component to perturbations in V_{SV}, as described by Latallerie, Zaroli, et al. (2025). Finite-frequency theory is more accurate than the great-circle approximation, and the volumetric nature of sensitivity kernels (Figure 2c) helps to stabilize the inversion (Zhou, 2009a; Zhou et al., 2004). Additionally, it allows us to image 3D structure in a single inversion step. We solve the inverse problem using the SOLA method (Zaroli, 2016; Zaroli et al., 2017), which provides control on resolution and uncertainty. The combination of finite-frequency theory with SOLA makes it possible to obtain resolution information in 3D, in contrast with earlier methods (e.g., Latallerie et al., 2022). More information can be found in the Supporting Information S1. We design a homogeneous target resolution throughout the model domain, aiming for a laterally isotropic resolution of 200 km in radius and 25 km vertically (e.g., pancake shape targets). We use a local parameterization with voxels of 2° × 2° × 25 km and invert only for cells where the data sensitivity (Figure 2d) is sufficiently large. e.g., at 112 km depth, we invert only for voxels in which the data sensitivity is above $\sim$10 rad km^{-3}.

3. Structure, Resolution and Uncertainty of the Pacific Uppermost Mantle According to SS3DPacific

By construction, the SOLA method provides model uncertainty and resolution together with the model estimate of $\delta \ln V_{SV}$ (Figures 3 and 4). Counter-intuitively, uncertainty is higher in regions with good data coverage, balanced by a good fit to the target resolution in these areas. High uncertainty spikes co-locate with isolated stations where data sampling different paths contradict one another. Resolution is generally well-focused laterally and circular. The resolution length, defined here as the 1-σ contour of the Gaussian that best fits the resolving kernel, is around 300–500 km in radius. Vertically, the resolution tends to be smeared down to greater depths for shallow targets, or to shallower depths for deeper targets, with the optimal resolution found around 87–112 km depth (Figure 4a).

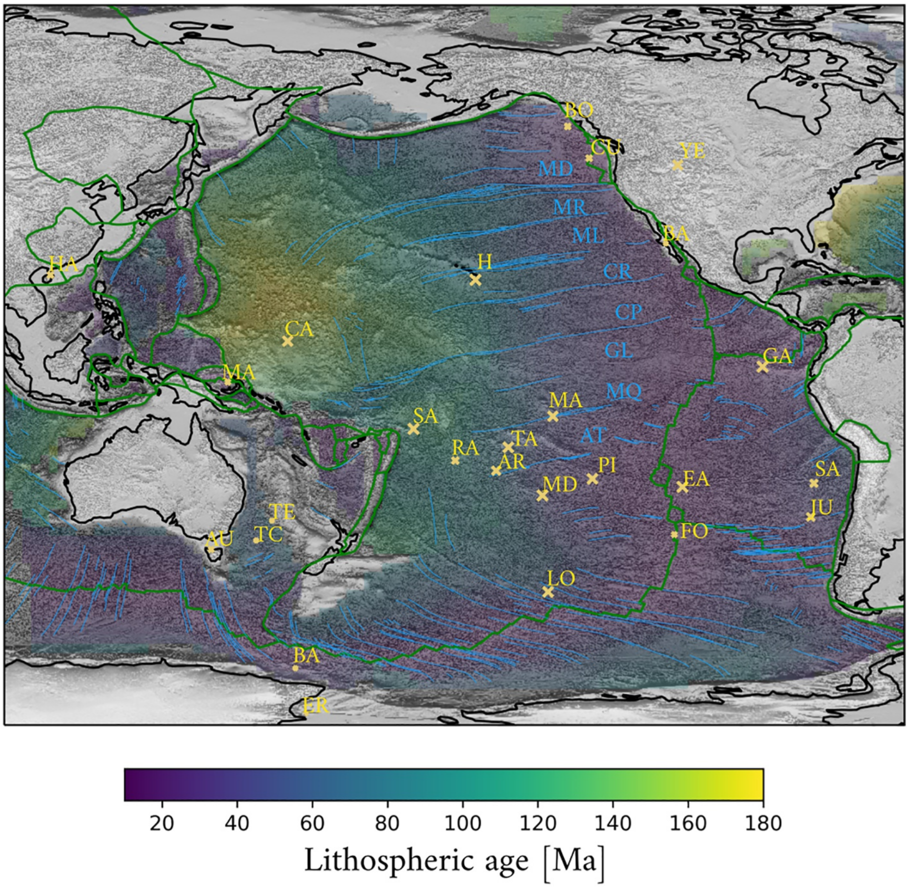

Figure 1. Map of the Pacific ocean and surrounding regions, showing the bathymetry (shaded background, from GEBCO Bathymetric Compilation Group, 2024, 2024), lithospheric age (colormap, from Seton et al., 2020), hotspot locations (yellow crosses, from Jackson et al., 2021), fracture zones (cyan lines, from Matthews et al., 2011), and plate boundaries (green lines, from Bird, 2003). The size of the cross scales with the likelihood for the hotspot to have a deep plume origin, consistent with the scoring approach of Koppers et al. (2021). Fracture zones are labeled in cyan (MD, Mendocino; MR, Murray; ML, Molokai; CR, Clarion; CP, Clipperton; GL, Galapagos; MQ, Marquesas; AT, Austral), and hotspots in yellow (BO, Bowie; GU, Guadeloupe; YE, Yellowstone; BA, Baja; GA, Galapagos; SA, San Felix; JU, Juan Fernandez; EA, Easter; FO, Foundation; LO, Louisville; ER, Erebus; BA, Balleny; AU, Australia; TC, Tasmanid Central; TE, Tasmanid Easter; MA, Manus; CA, Caroline; HA, Hanai; SA, Samoa; RA, Rarotonga; AR, Arago; TA, Tahiti; MD, Mac Donald; PI, Pitcairn; MA, Marquesas; H, Hawaii).

This strong vertical smearing, sometimes referred to as "depth leakage," is expected to have strong implications for interpretations of the depth of structures in the tomographic model, and should therefore be taken into account.

SS3DPacific agrees well with other recent tomography models (detailed in Table S1 of Supporting Information S1) in terms of large-scale velocity anomalies, such as the location of cratons, mid-oceanic ridges and the velocity gradient with distance from ridges (Figure S1 in Supporting Information S1). We also observe a good correlation between hotspot locations and low-velocity anomalies that stand out after we remove the lithosphere cooling trend and mask velocity anomalies that are not significant (see Figure S2 in Supporting Information S1), following the approach of Latallerie et al. (2022).

4. Age Cooling Trend

To investigate the cooling trend of the uppermost mantle, we interpolate the lithospheric age model of Seton et al. (2020) onto the tomographic grid (Figure 3d) and use this to compute the averaged $\delta \ln V_{SV}$ of SS3DPacific and other tomography models in 2 Ma age bins (Figure 5). To avoid any complexities in the analysis, we only consider cooling trends within the Pacific plate, far from plate boundaries, hotspots, and fracture zones (Figure S3 in Supporting Information S1). Following this procedure, we observe a wedge-like low-velocity region near the

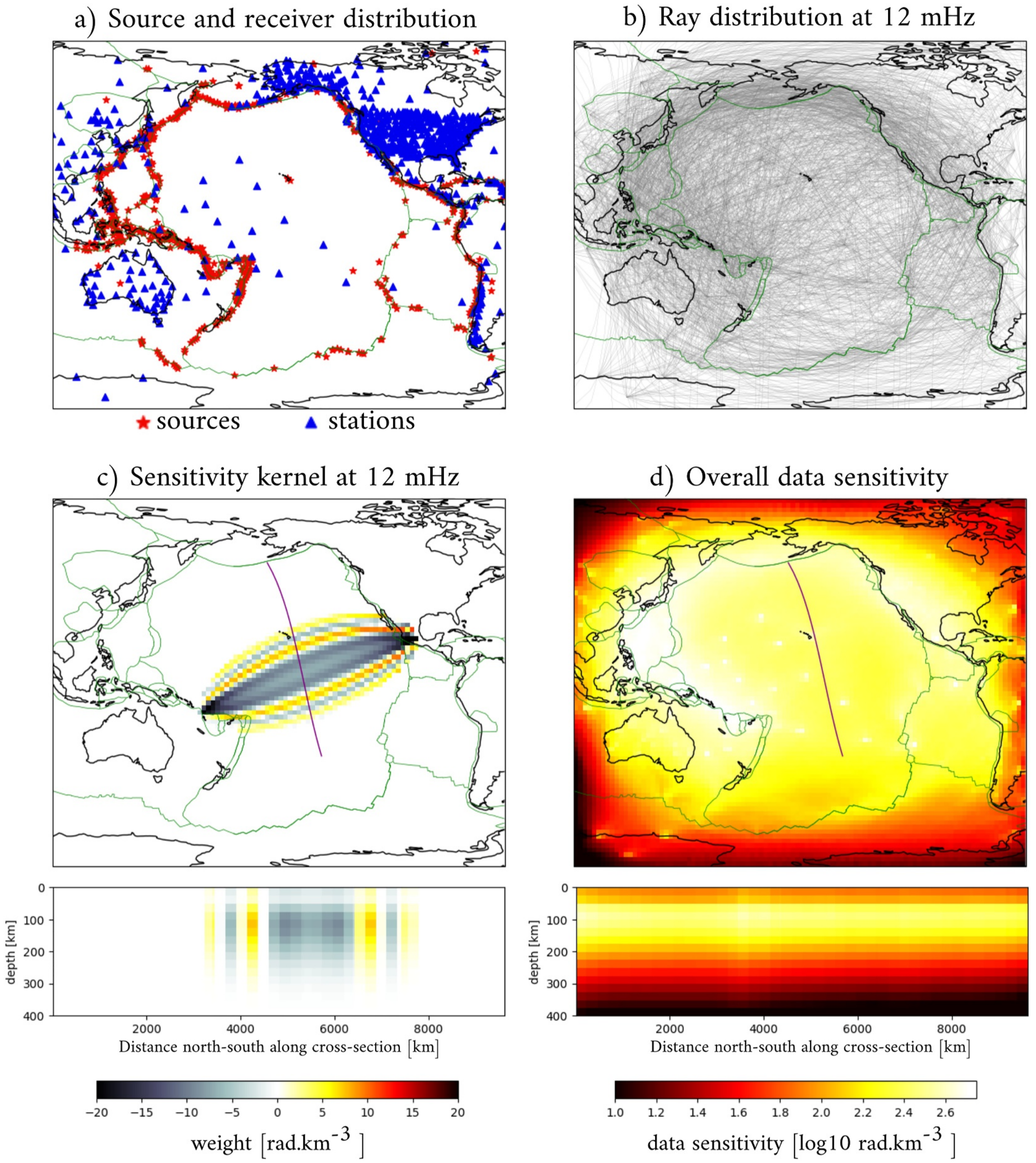

Figure 2. Data geometry and setup: (a) Source and receiver distribution, (b) Example ray distribution at 12 mHz, (c) Example sensitivity kernel at 12 mHz including a cross-section along the purple line, (d) Overall data sensitivity defined as $S_j = \log 10 \sum_i G_{ij}$, where $\boldsymbol{G}$ is the sensitivity matrix, with cross-section below. Maps of (c, d) are plotted at 112 km depth.

ridge that gradually deepens with age, before flattening (Figure 5), consistent with several other tomographic models.

We compare the trends of model SS3DPacific with predictions based on the HSC and PC models. For HSC, we compute the thermal structure using the analytical expression and constants from Stein and Stein (1992), whereas for PC we use the model of Richards et al. (2018). We apply the same age binning process as for the tomography. Throughout this analysis, we assume the 1175°C isotherm represents the base of the lithosphere-asthenosphere boundary, as suggested by Richards et al. (2018).

We should in principle convert the predicted temperatures into velocities. However, such conversions require several assumptions that introduce subjectivity, which we prefer to avoid here. Therefore, we only analyze the geometrical effect of resolution on the temperature predictions, but we believe that this effect will also affect seismic velocities. Particularly, the predicted, large-scale seismic velocity structure will resemble the thermal

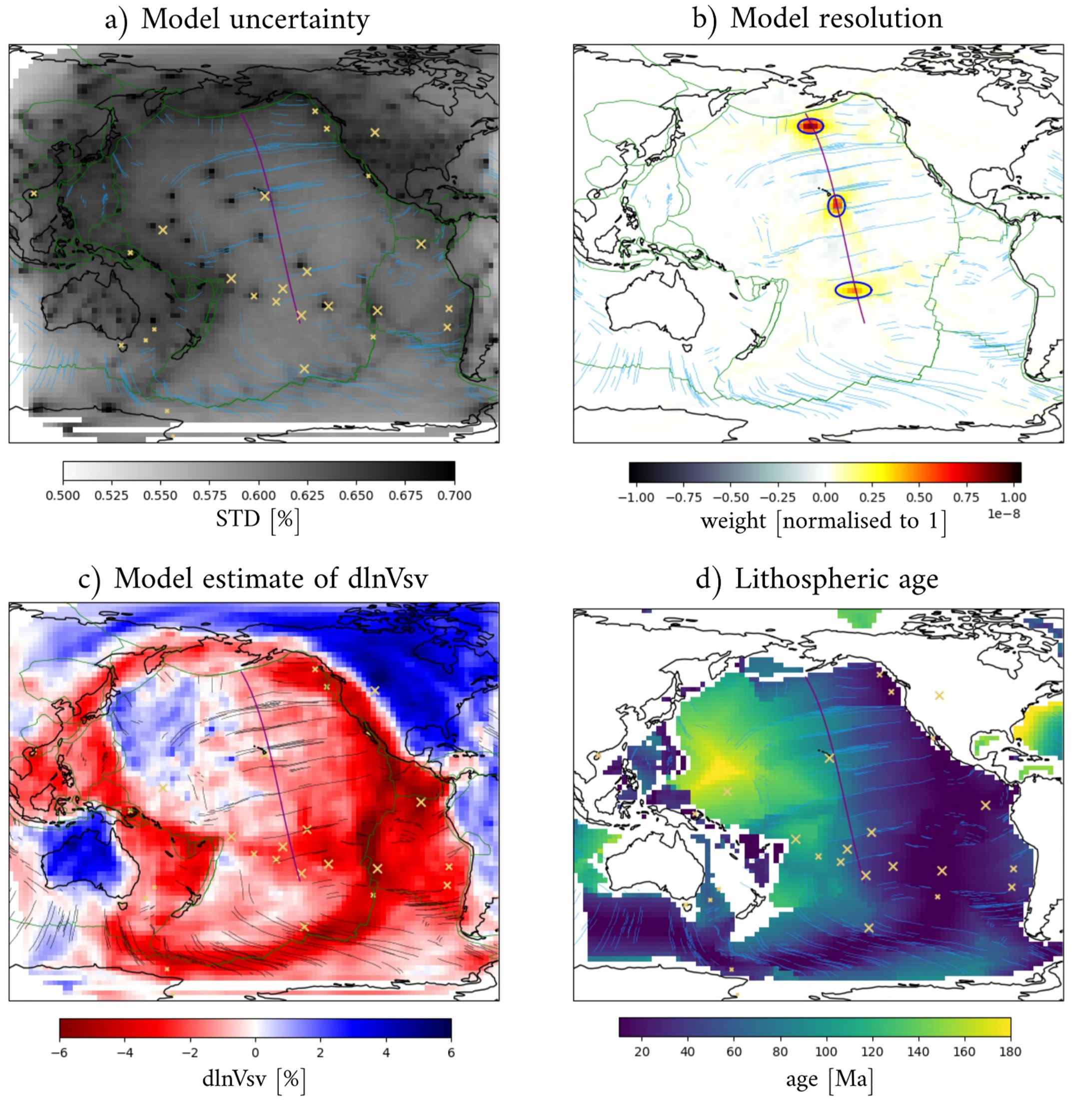

Figure 3. Model SS3DPacific at 112 km depth, showing (a) Model uncertainty; (b) Example resolution kernels for 3 selected locations; (c) Model estimates of $\delta \ln V_{SV}$; and (d) Age of the lithosphere in Ma. For the resolution kernels in panel (b), the blue ellipses indicate the 1-σ contour of the best fitting Gaussian. The purple line indicates the location of the cross-sections shown in Figure 4. Yellow crosses indicate hotspots, and cyan (or black) lines fracture zones.

structure (a set of isotherms would behave similarly to isotachs with age, at least to some extent). Nevertheless, the reader should keep in mind that temperature-velocity conversions potentially affect our conclusions, especially for temperatures close to the solidus where non-linear effects become important (e.g., Yamauchi & Takei, 2016).

To compare the observed and predicted age trends, we need to account for the limited tomographic resolution, for example, "tomographically filter" the temperature predictions (see the Supporting Information S1 for more information). Our study is unique in that we can apply the resolution provided by SOLA to the HSC and PC predictions (solid lines in Figure 5 and Figure S4 in Supporting Information S1). Note that any meaningful comparison between thermal cooling models and tomographic results should use the filtered predictions of the cooling models. Tomographic filtering allows us to account for the vertical resolution smearing, which is crucial for interpreting structures such as the lithosphere-asthenosphere boundary. Figure 5 demonstrates that the filtering of HSC and PC predictions produces a similar isotherm "wedge" shape as observed in the velocity structure of SS3DPacific. The filtering thus changes the geometry of the isotherms (i.e., inferred cooling), though the very shallow part of the model is less distorted. In particular, filtering creates a positive velocity gradient with depth at

a) Cross-section through SS3DPacific

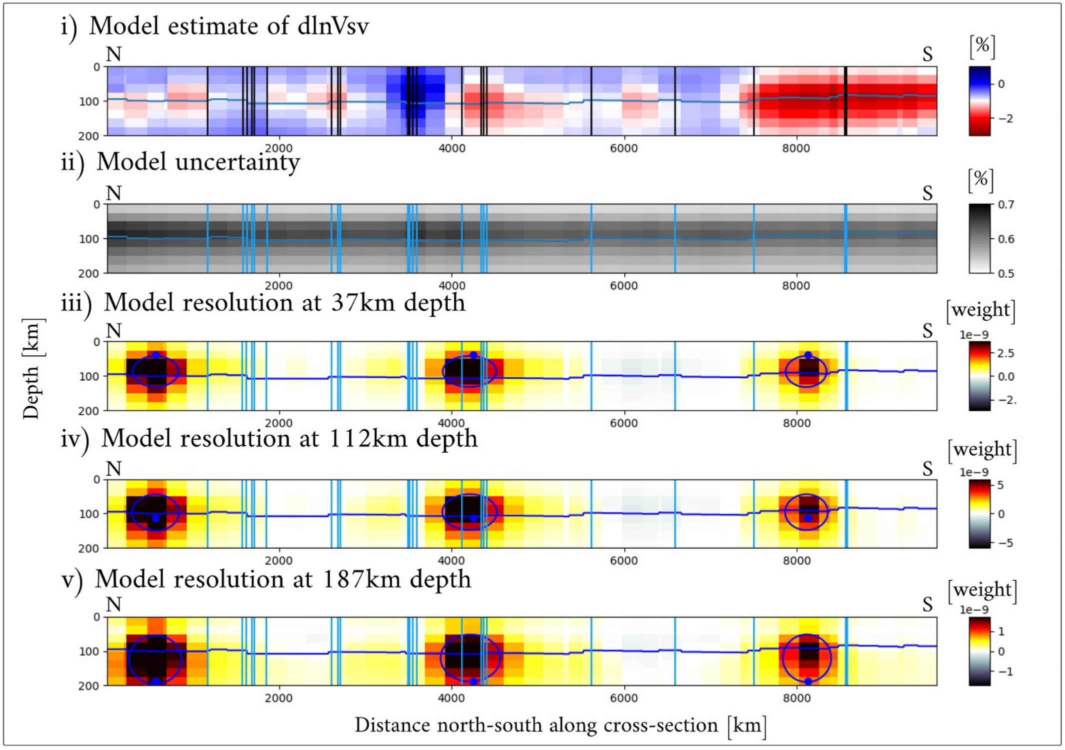

i) Model estimate of dlnVsv

ii) Model uncertainty

iii) Model resolution at 37km depth

iv) Model resolution at 112km depth

v) Model resolution at 187km depth

b) Relationship between age and seismic velocity

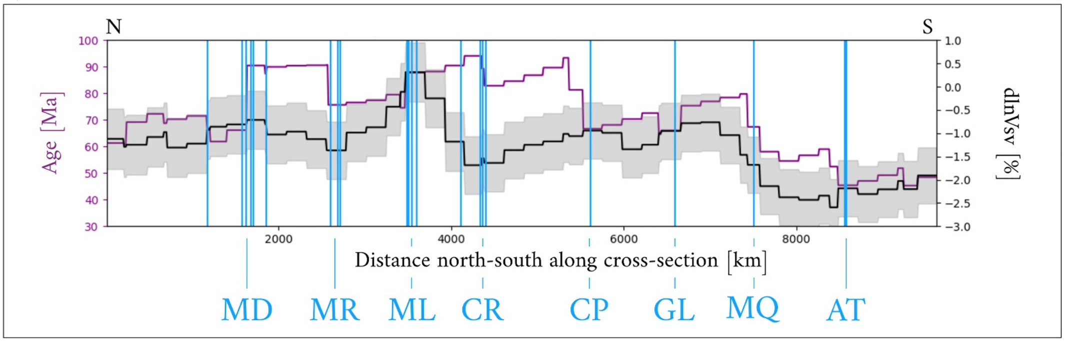

Figure 4. Model SS3DPacific compared to lithospheric age. (a) Cross-sections through SS3DPacific along the purple line in Figure 3 showing (i) Model estimate of $\delta \ln V_{SV}$, (ii) Model uncertainty, (iii–v) Example resolution kernels for target kernels centered at 37, 112, and 187 km depth respectively, at the same locations as in Figure 3b as represented by blue dots. Blue ellipses indicate in each case the 1-σ contour of the best fitting Gaussian. The blue lines represent the depth of the 1175°C isotherm in the PC model. (b) Lithospheric age (purple) compared to model estimate of $\delta \ln V_{SV}$ at 112 km depth (black line with gray bands representing the 1-σ uncertainty). The vertical cyan (or black) lines indicate fracture zones (see Figure 1).

the lower boundary of the wedge (near the bottom of the models in Figure 5), which could mistakenly be interpreted as the base of the asthenosphere in surface-wave tomographic models. Since this wedge-shape geometry of low-velocities is also present in other tomographic models, these may also suffer from similar vertical resolution smearing. However, we cannot investigate this in detail, given full 3D resolution information is generally not available for other published models.

While the difference between the original predictions of the HSC and PC models (dashed lines) is small, filtering makes them appear even more similar (solid lines). This is not only true for the 1,175°C isotherm shown in Figure 5, but also for the overall age-depth structure (Figure S4 in Supporting Information S1). This makes the cooling models more difficult to distinguish using surface-wave tomography, though the geometry of their difference remains similar. In particular, the flattening with age of the PC model appears weaker after filtering,

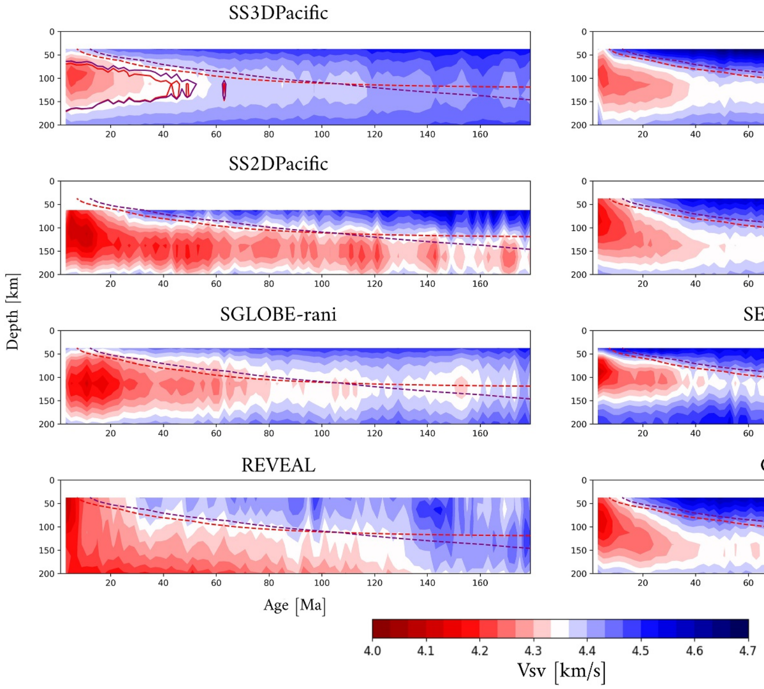

Figure 5. V_{SV} structure of SS3DPacific compared to other seismic tomography models, averaged in 2 Ma age bins. Purple and red dashed lines represent the 1175°C isotherm of the HSC and PC models, respectively. For SS3DPacific, we also include the filtered versions that account for the limited resolution (solid lines). Only the filtered version of the cooling models (solid lines or filtered HSC or PC on Figure S4 in Supporting Information S1) should be directly compared to SS3DPacific. We include tomography models SS2DPacific (Latallerie et al., 2022), SGLOBE-rani (Chang et al., 2015), REVEAL (Thrastarson et al., 2024), FFSW1 (Zhou et al., 2006), S362ANI (Kustowski et al., 2008), SEMUCB-WM1 (French & Romanowicz, 2014), and GLAD-M35 (Cui et al., 2024).

diminishing the diagnostic difference between the HSC and PC models. The strong sensitivity of seismic velocity to temperature may exacerbate differences between the HSC and PC models if their temperature predictions are converted into velocities (Yamauchi & Takei, 2016). To investigate this, temperature-velocity conversions would need to be performed and residual misfits in the velocity structure could be compared to the tomographic uncertainties. Nevertheless, our resolution analysis shows that it is vital to take into account vertical resolution smearing in surface-wave tomography when interpreting imaged structures in terms of lithospheric cooling.

5. Fracture Zones

Besides the main features in SS3DPacific (see Section 3), we observe an interesting pattern of anomalous bands aligned with major fracture zones in the North West and Equatorial Pacific (see Figures 3 and 4i). This is most pronounced around the depth of the lithosphere-asthenosphere boundary as predicted by the 1175°C isotherm of the PC model. The peak-to-peak difference in $\delta \ln V_{SV}$ between the bands is ~3%, which is above the average model uncertainty in this region of ~0.7% (Figure 4ii). The bands are spaced roughly ~800 km apart, thus resolvable given the lateral resolution length of ~450 km in this region (Figures 4iii–4v). The resolution is laterally also very isotropic here (Figure 3b), implying that these bands do not arise from a lateral resolution smearing effect. As we applied crustal corrections to the data, it is also unlikely to arise from a leakage of crustal structure down to the upper mantle. To further reinforce this argument, we repeat our SOLA inferences for $\delta \ln V_{SV}$ structure without the crustal correction, as well as for $\delta \ln V_{SV}$ structure that only arises from the crustal correction term (Figure S5 in Supporting Information S1). The banded pattern is already visible in the model without crustal correction (Figure S5a in Supporting Information S1). Our tests indicate that the banded pattern is not introduced or reinforced by the crustal correction (Figure S5b in Supporting Information S1). However, the crust could still cause the bands if the crustal model, or the crustal correction strategy, is insufficient for removing the crustal effect.

To the best of our knowledge, this banded pattern at lithosphere-asthenosphere boundary depths has not been seen or interpreted in existing tomography models (Figure S1 in Supporting Information S1). We argue that we can resolve it in SS3DPacific thanks to the combined use of finite-frequency theory and SOLA inferences. The detailed sensitivity in the volumetric sensitivity kernels (Figure 2c) adds physical information, explaining why we are able to obtain a coherent Pacific-wide model with only 44,917 measurements, compared with state-of-the-art surface-wave tomographic studies that typically use millions of measurements. The SOLA method is also able to extract relevant information from the data at every target location. Particularly, by designing the target kernels, we have prioritized a larger, but isotropic resolution over a smaller, but highly anisotropic and complex resolution.

Models for the cooling of the lithosphere usually assume a laterally infinite plate, only accounting for vertical diffusion of heat. Scaling analysis indicates that lateral diffusion in the direction of plate motion can be neglected (Parsons & Sclater, 1977), and that no diffusion is expected perpendicular to this if the temperature is constant. However, fracture zones produce lateral offsets in lithospheric age and thus thermal structure that are likely incompatible with these assumptions. The fact that we observe the banded pattern in SS3DPacific indicates that lateral diffusion of heat across fracture zones is not strong enough to smooth out the age (and thus thermal) offsets. Further investigation of this would require a numerical model of the thermal structure including offsets in the lithospheric age, and a comparison to the banded pattern observed in SS3DPacific. In turn, the tomographic observations could be used as new constraints on the parameters of such modeling of the oceanic lithosphere.

In the southern part of the cross-section (Figure 4), the anomalous bands appear to follow a consistent, expected relationship between age and wavespeed (younger lithosphere being slower and older lithosphere being faster). However, in the northern part (between the Mendocino and Clipperton fracture zones), we note a more complex relationship. While uncertainty and resolution limit our ability to interpret these trends, it suggests that additional non-negligible physical processes may occur at the fracture zones themselves. This is supported by other work that suggests that important changes in the structure of the lithosphere might occur at fracture zones. For example, the nature of volcanism along volcanic arcs has been observed to vary above subducted fracture zones (Manea et al., 2014), fracture zones appear to be more seismically active than thought (Bohnenstiehl et al., 2004), and may have higher heat flow than the average oceanic domain (Gregory et al., 2023). More relevant to this work, they may be subject to fluid movements, hydration, metasomatism and water induced melting (Schmeling et al., 2017), potentially leading to local thinning of the lithosphere (Wang et al., 2022). However, it is difficult to explain the faster bands based on these processes. Alternatively, the bands may be the signature of small-scale convection that nucleates from instabilities triggered by age offsets at fracture zones (Dumoulin et al., 2004; Huang et al., 2003), which could explain both low and fast velocity anomalies. While these processes occur on shorter spatial scales than SS3DPacific can resolve, it is clear that the observed banded pattern in $\delta \ln V_{SV}$ hints at complexities in the structure of the lithosphere across fracture zones.

6. Discussion and Concluding Remarks

Resolution and uncertainties allow us to quantitatively assess the robustness of different features and to compare SS3DPacific to model predictions of lithospheric cooling. Our new framework makes it possible to account for 3D resolution (Latallerie, Zaroli, et al., 2025), in contrast to previous lateral, 2D approaches, opening up novel discussions about vertical resolution effects in surface-wave tomography. Resolution analysis shows that strong vertical resolution smearing makes it harder to distinguish cooling models, a limitation that is likely shared with other surface-wave tomography models. A clear step forward would be the inclusion of overtones in our methodology, to better illuminate deeper mantle structure and thus potentially reduce the vertical resolution smearing. While some other tomography models do include overtone data (see Table S1 in Supporting Information S1), in the absence of resolution information for these, it is difficult to assess at present whether these data reduce the vertical resolution smearing sufficiently to discriminate between the two cooling models.

Laterally, SS3DPacific features a pattern of anomalous bands aligned with oceanic fracture zones that produce offsets in the age of the lithosphere. That we still observe the bands at older ages indicates weak lateral heat transfer across fracture zones. Thermal modeling including lateral heat diffusion across fracture zones would help to better understand the physical characteristics of the lithosphere. Particularly, not all fracture zones have the same seismic signature; some align with velocity lows, others with velocity highs, reflecting possibly that different mechanisms occur at the fracture zones. If fracture zones represented pathways for fluids, such as melt or water, the lithosphere along fracture zones may reheat and be rejuvenated or undergo cooling and metasomatism, respectively. Alternatively, age offsets may help to trigger small-scale convection.

To better investigate processes occurring at fracture zones, new seismic constraints could be derived using the same approach as here. In particular, mapping both V_P and V_S with the same local resolution (Restelli et al., 2024; Serra et al., 2025) to obtain robust V_P/V_S ratios could provide constraints on enrichment in serpentine along fracture zones. Imaging radial anisotropy through joint inversion of Love and Rayleigh waves would also provide constraints on fracture alignments along fracture zones. Finally, mapping attenuation would make it possible to map melt migration across the fracture zones.

The age-dependent structure of the oceanic lithosphere remains to be explored. Lateral complexities in the lithospheric structure indicate that fracture zones may play a significant role. Detailed seismological images with better resolution (laterally and vertically) will be needed to unravel the complex cooling history of the oceanic lithosphere. Such images will have to be accompanied by robust uncertainty and resolution information to ensure interpretations are free from methodological biases.

Conflict of Interest

The authors declare no conflicts of interest relevant to this study.

Data Availability Statement

Seismic source solutions were downloaded from the Global Centroid Moment Tensor (GCMT) Catalog (Dziewonski et al., 1981; Ekström et al., 2012). The facilities of the EarthScope Consortium were used to access waveforms and related metadata and derived data products. These services are funded through the National Science Foundation's Seismological Facility for the Advancement of Geoscience (SAGE) Award under Cooperative Agreement EAR-1724509. Citations for networks used are provided in the Supporting Information S1. To compute the finite-frequency sensitivity kernels, we used software provided by Ying Zhou (2009b), available via their webpage (http://seismo.geos.vt.edu/software.html). To compute the reference seismograms in a 1D radial Earth model, we used normal modes summation as implemented in MINEOS 1.0.2 (Masters et al., 2011) published under the GPL2 license. We thank the Computational Infrastructure for Geodynamics (http://geodynamics.org), which is funded by the National Science Foundation under awards EAR-0949446, EAR-1550901, and EAR-2149126, for making the code available. The SOLA tomography code used in this study consists of running the LSQR algorithm of Paige and Saunders (1982) with specific input matrices and vectors. These inputs can be constructed from the sensitivity matrix and target kernels as detailed in Appendix A1 of (Zaroli, 2016). The LSQR code is freely downloadable from the webpage of the Systems Optimisation Laboratory (Stanford University): https://web.stanford.edu/group/SOL/software/lsqr/. A pre-constructed software package for finite-frequency surface-wave SOLA tomography is available at Latallerie, Zaroli, et al. (2025a). We made extensive use of Ubuntu 20.04.6 LTS (https://ubuntu.com/), Python packages Numpy (Harris et al., 2020), Scipy (Virtanen et al., 2020), Pandas (The pandas development team, 2023, and Matplotlib (Hunter, 2007). The surface-wave phase-delay measurements, SS3DPacific model files, and plotting scripts are available at Latallerie, Koelemeijer, et al. (2025).

Acknowledgments

We thank the editor, Germán Prieto, as well as Eric Debayle and an anonymous reviewer for their comments that improved our manuscript. This research was supported by the UKRI NERC Large grant "Mantle Circulation Constrained (MC2): A multidisciplinary 4D Earth framework for understanding mantle upwellings" (NE/T01248X/1 and NE/T012684/1). FL and PK also acknowledge financial support from the Royal Society (URF\R1\180377 and RF\ERE\231085). CZ acknowledges financial support from ITES (Institut Terre et Environnement de Strasbourg, UMR 7063) for a research visit to Oxford. This study used the ARCHER2 UK National Supercomputing Service (https://www.archer2.ac.uk). For the purpose of open access, the authors have applied a CC BY public copyright license to any Author Accepted Manuscript version arising.

References

An, M. (2012). A simple method for determining the spatial resolution of a general inverse problem. *Geophysical Journal International*, *191*(2), 849–864. https://doi.org/10.1111/j.1365-246X.2012.05661.x

Auer, L., Boschi, L., Becker, T. W., Nissen-Meyer, T., & Giardini, D. (2014). *Savani*: A variable resolution whole-mantle model of anisotropic shear velocity variations based on multiple data sets. *Journal of Geophysical Research: Solid Earth*, *119*(4), 3006–3034. https://doi.org/10.1002/2013JB010773

Backus, G., & Gilbert, F. (1968). The resolving power of gross Earth data. *Geophysical Journal International*, *16*(2), 169–205. https://doi.org/10.1111/j.1365-246X.1968.tb00216.x

Ballmer, M. D., van Hunen, J., Ito, G., Bianco, T. A., & Tackley, P. J. (2009). Intraplate volcanism with complex age-distance patterns: A case for small-scale sublithospheric convection: Intraplate volcanism from small-scale convection. *Geochemistry, Geophysics, Geosystems*, *10*(6). https://doi.org/10.1029/2009GC002386

Bassin, C., Laske, G., & Masters, G. (2000). The current limits of resolution for surface wave tomography in North America. *Eos, Transactions American Geophysical Union*, *81*(F897).

Bird, P. (2003). An updated digital model of plate boundaries: Updated model of plate boundaries. *Geochemistry, Geophysics, Geosystems*, *4*(3). https://doi.org/10.1029/2001GC000252

Bohnenstiehl, D. R., Tolstoy, M., & Chapp, E. (2004). Breaking into the plate: A 7.6 Mw fracture-zone earthquake adjacent to the central Indian Ridge. *Geophysical Research Letters*, *31*(2), 2003GL018981. https://doi.org/10.1029/2003GL018981

Chang, S.-J., Ferreira, A. M. G., Ritsema, J., van Heijst, H. J., & Woodhouse, J. H. (2015). Joint inversion for global isotropic and radially anisotropic mantle structure including crustal thickness perturbations: Radially anisotropic mantle structure. *Journal of Geophysical Research: Solid Earth*, *120*(6), 4278–4300. https://doi.org/10.1002/2014JB011824

Cui, C., Lei, W., Liu, Q., Peter, D., Bozdağ, E., Tromp, J., et al. (2024). GLAD-M35: A joint P and S global tomographic model with uncertainty quantification. *Geophysical Journal International*, *239*(1), 478–502. https://doi.org/10.1093/gji/ggae270

Dumoulin, C., Doin, M.-P., Arcay, D., & Fleitout, L. (2004). Onset of small-scale instabilities at the base of the lithosphere: Scaling laws and role of pre-existing lithospheric structures: Onset of sublithospheric convection. *Geophysical Journal International*, *160*(1), 345–357. https://doi.org/10.1111/j.1365-246X.2004.02475.x

Dziewonski, A. M., Chou, T.-A., & Woodhouse, J. H. (1981). Determination of earthquake source parameters from waveform data for studies of global and regional seismicity. *Journal of Geophysical Research*, *86*(B4), 2825–2852. https://doi.org/10.1029/JB086iB04p02825

Ekström, G., Nettles, M., & Dziewoński, A. (2012). The global CMT project 2004–2010: Centroid-moment tensors for 13,017 earthquakes. *Physics of the Earth and Planetary Interiors*, *200–201*, 1–9. https://doi.org/10.1016/j.pepi.2012.04.002

Fichtner, A., & Trampert, J. (2011). Resolution analysis in full waveform inversion: Resolution in full waveform inversion. *Geophysical Journal International*, *187*(3), 1604–1624. https://doi.org/10.1111/j.1365-246X.2011.05218.x

Freissler, R., Schuberth, B. S. A., & Zaroli, C. (2024). A concept for the global assessment of tomographic resolution and uncertainty. *Geophysical Journal International*, *238*(2), ggae178–1012. https://doi.org/10.1093/gji/ggae178

French, S., Lekic, V., & Romanowicz, B. (2013). Waveform tomography reveals channeled flow at the base of the Oceanic asthenosphere. *Science*, *342*(6155), 227–230. https://doi.org/10.1126/science.1241514

French, S. W., & Romanowicz, B. A. (2014). Whole-mantle radially anisotropic shear velocity structure from spectral-element waveform tomography. *Geophysical Journal International*, *199*(3), 1303–1327. https://doi.org/10.1093/gji/ggu334

GEBCO Bathymetric Compilation Group 2024. (2024). *The GEBCO_2024 grid—A continuous terrain model of the global oceans and land*. NERC EDS British Oceanographic Data Centre NOC. https://doi.org/10.5285/1C44CE99-0A0D-5F4F-E063-7086ABC0EA0F

Gregory, E. P. M., Villinger, H., Singh, S. C., & Kaul, N. (2023). High heat flow anomaly within the St Paul fracture zone: Heat advection and/or inherent thermal structure? *Geochemistry, Geophysics, Geosystems*, *24*(4), e2022GC010385. https://doi.org/10.1029/2022GC010385

Harris, C. R., Millman, K. J., Walt, S. J. V. D., Gommers, R., Virtanen, P., Cournapeau, D., et al. (2020). Array programming with NumPy. *Nature*, *585*(7825), 357–362. https://doi.org/10.1038/s41586-020-2649-2

Huang, J., Zhong, S., & Van Hunen, J. (2003). Controls on sublithospheric small-scale convection. *Journal of Geophysical Research*, *108*(B8), 2003JB002456. https://doi.org/10.1029/2003JB002456

Hunter, J. D. (2007). Matplotlib: A 2D graphics environment. *Computing in Science and Engineering*, *9*(3), 90–95. https://doi.org/10.1109/MCSE.2007.55

Isse, T., Kawakatsu, H., Yoshizawa, K., Takeo, A., Shiobara, H., Sugioka, H., et al. (2019). Surface wave tomography for the Pacific Ocean incorporating seafloor seismic observations and plate thermal evolution. *Earth and Planetary Science Letters*, *510*, 116–130. https://doi.org/10.1016/j.epsl.2018.12.033

Jackson, M. G., Becker, T. W., & Steinberger, B. (2021). Spatial characteristics of recycled and primordial reservoirs in the deep mantle. *Geochemistry, Geophysics, Geosystems*, *22*(3), e2020GC009525. https://doi.org/10.1029/2020GC009525

Koppers, A. A. P., Becker, T. W., Jackson, M. G., Konrad, K., Müller, R. D., Romanowicz, B., et al. (2021). Mantle plumes and their role in Earth processes. *Nature Reviews Earth and Environment*, *2*(6), 382–401. https://doi.org/10.1038/s43017-021-00168-6

Korenaga, T., Korenaga, J., Kawakatsu, H., & Yamano, M. (2021). A new reference model for the evolution of Oceanic lithosphere in a cooling Earth. *Journal of Geophysical Research: Solid Earth*, *126*(6), e2020JB021528. https://doi.org/10.1029/2020JB021528

Kustowski, B., Ekström, G., & Dziewoński, A. M. (2008). Anisotropic shear-wave velocity structure of the Earth's mantle: A global model. *Journal of Geophysical Research*, *113*(B6), B06306. https://doi.org/10.1029/2007JB005169

Latallerie, F., Koelemeijer, P., Walker, A., Lambotte, S., Maggi, A., & Zaroli, C. (2025). Rayleigh wave phase delays and Vsv upper-mantle structure in the Pacific [Dataset]. *NERC EDS National Geoscience Data Centre*. https://doi.org/10.5285/17fd6862-c3e8-4fb4-a33d-64c1cedc2d3f

Latallerie, F., Zaroli, C., Lambotte, S., & Maggi, A. (2022). Analysis of tomographic models using resolution and uncertainties: A surface wave example from the Pacific. *Geophysical Journal International*, *230*(2), 893–907. https://doi.org/10.1093/gji/ggac095

Latallerie, F., Zaroli, C., Lambotte, S., Maggi, A., Walker, A., & Koelemeijer, P. (2025). SOLA_ffsw [Software]. *Zenodo*. https://doi.org/10.5281/zenodo.17245074

Latallerie, F., Zaroli, C., Lambotte, S., Maggi, A., Walker, A., & Koelemeijer, P. (2025). Towards surface wave tomography with 3D resolution and uncertainty: Resolution-uncertainty in 3D surface-wave tomography. *Seismica*, *4*(2). https://doi.org/10.26443/seismica.v4i2.1407

Maggi, A., Debayle, E., Priestley, K., & Barruol, G. (2006). Multimode surface waveform tomography of the Pacific Ocean: A closer look at the lithospheric cooling signature. *Geophysical Journal International*, *166*(3), 1384–1397. https://doi.org/10.1111/j.1365-246X.2006.03037.x

Manea, V. C., Leeman, W. P., Gerya, T., Manea, M., & Zhu, G. (2014). Subduction of fracture zones controls mantle melting and geochemical signature above slabs. *Nature Communications*, *5*(1), 5095. https://doi.org/10.1038/ncomms6095

Masters, G., Woodhouse, J. H., & Freeman, G. (2011). Mineos v1.0.2 [Software]. *Computational Infrastructure for Geodynamics*. Retrieved from https://geodynamics.org/cig

Matthews, K. J., Müller, R. D., Wessel, P., & Whittaker, J. M. (2011). The tectonic fabric of the ocean basins. *Journal of Geophysical Research*, *116*(B12), B12109. https://doi.org/10.1029/2011JB008413

McKenzie, D. P. (1967). Some remarks on heat flow and gravity anomalies. *Journal of Geophysical Research*, *72*(24), 6261–6273. https://doi.org/10.1029/jz072i024p06261

Nolet, G., Montelli, R., & Virieux, J. (1999). Explicit, approximate expressions for the resolution and *a posteriori* covariance of massive tomographic systems. *Geophysical Journal International*, *138*(1), 36–44. https://doi.org/10.1046/j.1365-246x.1999.00858.x

Paige, C. C., & Saunders, M. A. (1982). LSQR: An algorithm for sparse linear equations and sparse least squares. *ACM Transactions on Mathematical Software*, *8*(1), 43–71. https://doi.org/10.1145/355984.355989

Parsons, B., & Sclater, J. G. (1977). An analysis of the variation of ocean floor bathymetry and heat flow with age. *Journal of Geophysical Research*, *82*(5), 803–827. https://doi.org/10.1029/JB082i005p00803

Pijpers, F. P., & Thompson, M. J. (1994). The SOLA method for helioseismic inversion. *Astronomy and Astrophysics*, *281*, 231–240.

Rawlinson, N., Fichtner, A., Sambridge, M., & Young, M. (2014). Seismic tomography and the assessment of uncertainty. *Advances in Geophysics*, *55*, 1–76. https://doi.org/10.1016/bs.agph.2014.08.001

Restelli, F., Zaroli, C., & Koelemeijer, P. (2024). Robust estimates of the ratio between S- and P-wave velocity anomalies in the Earth's mantle using normal modes. *Physics of the Earth and Planetary Interiors*, *347*, 107135. https://doi.org/10.1016/j.pepi.2023.107135

Richards, F., Hoggard, M., Cowton, L. R., & White, N. (2018). Reassessing the thermal structure of Oceanic lithosphere with revised global inventories of basement depths and heat flow measurements. *Journal of Geophysical Research: Solid Earth*, *123*(10), 9136–9161. https://doi.org/10.1029/2018JB015998

Richards, F., Hoggard, M., Crosby, A., Ghelichkhan, S., & White, N. (2020). Structure and dynamics of the Oceanic lithosphere-asthenosphere system. *Physics of the Earth and Planetary Interiors*, *309*, 106559. https://doi.org/10.1016/j.pepi.2020.106559

Richardson, W. P., Stein, S., Stein, C. A., & Zuber, M. T. (1995). Geoid data and thermal structure of the Oceanic lithosphere. *Geophysical Research Letters*, *22*(14), 1913–1916. https://doi.org/10.1029/95GL01595

Ritsema, J., & Lekić, V. (2020). Heterogeneity of seismic wave velocity in earth's mantle. *Annual Review of Earth and Planetary Sciences*, *48*(1), 377–401. https://doi.org/10.1146/annurev-earth-082119-065909

Ritsema, J., McNamara, A. K., & Bull, A. L. (2007). Tomographic filtering of geodynamic models: Implications for model interpretation and large-scale mantle structure. *Journal of Geophysical Research*, *112*(B01303). https://doi.org/10.1029/2006JB004566

Ritzwoller, M. H., Shapiro, N. M., & Zhong, S.-J. (2004). Cooling history of the Pacific lithosphere. *Earth and Planetary Science Letters*, *226*(1–2), 69–84. https://doi.org/10.1016/j.epsl.2004.07.032

Schmeling, H., Marquart, G., & Nawa, V. (2017). The role of hydrothermal cooling of the Oceanic lithosphere for ocean floor bathymetry and heat flow: Hydrothermal cooling of lithosphere. *Journal of Geophysical Research: Solid Earth*, *122*(5), 3934–3952. https://doi.org/10.1002/2016JB013881

Serra, E., Zaroli, C., Lambotte, S., & Koelemeijer, P. (2025). Inference of the *S* - To *P* -wave velocity anomalies ratio and its uncertainty with an application to south-east Asia. *Geophysical Journal International*, *244*(1), ggaf468. https://doi.org/10.1093/gji/ggaf468

Seton, M., Müller, R. D., Zahirovic, S., Williams, S., Wright, N. M., Cannon, J., & McGirr, R. (2020). A global data set of present-day Oceanic crustal age and seafloor spreading parameters. *Geochemistry, Geophysics, Geosystems*, *21*(10). https://doi.org/10.1029/2020gc009214

Snieder, R. (1986). 3-D linearized scattering of surface waves and a formalism for surface wave holography. *Geophysical Journal International*, *84*(3), 581–605. https://doi.org/10.1111/j.1365-246X.1986.tb04372.x

Stein, C. A., & Stein, S. (1992). A model for the global variation in Oceanic depth and heat flow with lithospheric age.

The pandas development team. (2023). Pandas v2.0.3 [Software]. *Zenodo*. https://doi.org/10.5281/zenodo.8092754

Thrastarson, S., Van Herwaarden, D.-P., Noe, S., Josef Schiller, C., & Fichtner, A. (2024). REVEAL: A global full-waveform inversion model. *Bulletin of the Seismological Society of America*, *114*(3), 1392–1406. https://doi.org/10.1785/0120230273

Virtanen, P., Gommers, R., Oliphant, T. E., Haberland, M., Reddy, T., Cournapeau, D., & SciPy 1.0 Contributors. (2020). SciPy 1.0: Fundamental algorithms for scientific computing in python. *Nature Methods*, *17*(3), 261–272. https://doi.org/10.1038/s41592-019-0686-2

Wang, Z., Singh, S. C., Prigent, C., Gregory, E. P. M., & Marjanović, M. (2022). Deep hydration and lithospheric thinning at Oceanic transform plate boundaries. *Nature Geoscience*, *15*(9), 741–746. https://doi.org/10.1038/s41561-022-01003-3

Wessel, P., & Haxby, W. F. (1990). Thermal stresses, differential subsidence, and flexure at Oceanic fracture zones. *Journal of Geophysical Research*, *95*(B1), 375–391. https://doi.org/10.1029/JB095iB01p00375

Yamauchi, H., & Takei, Y. (2016). Polycrystal anelasticity at near-solidus temperatures. *Journal of Geophysical Research: Solid Earth*, *121*(11), 7790–7820. https://doi.org/10.1002/2016JB013316

Zaroli, C. (2016). Global seismic tomography using backus-gilbert inversion. *Geophysical Journal International*, *207*(2), 876–888. https://doi.org/10.1093/gji/ggw315

Zaroli, C., Koelemeijer, P., & Lambotte, S. (2017). Toward seeing the earth's interior through unbiased tomographic lenses. *Geophysical Research Letters*, *44*(22), 11399–11408. https://doi.org/10.1002/2017GL074996

Zhou, Y. (2009a). Multimode surface wave sensitivity kernels in radially anisotropic Earth media. *Geophysical Journal International*, *176*(3), 865–888. https://doi.org/10.1111/j.1365-246X.2008.04010.x

Zhou, Y. (2009b). Surface-wave sensitivity to 3-D anelasticity. *Geophysical Journal International*, *178*(3), 1403–1410. https://doi.org/10.1111/j.1365-246X.2009.04230.x

Zhou, Y., Dahlen, F. A., & Nolet, G. (2004). Three-dimensional sensitivity kernels for surface wave observables. *Geophysical Journal International*, *158*(1), 142–168. https://doi.org/10.1111/j.1365-246X.2004.02324.x

Zhou, Y., Nolet, G., Dahlen, F. A., & Laske, G. (2006). Global upper-mantle structure from finite-frequency surface-wave tomography. *Journal of Geophysical Research*, *111*(B04304). https://doi.org/10.1029/2005JB003677

References From the Supporting Information

Alaska Earthquake Center, Univ. of Alaska Fairbanks. (1987). Alaska geophysical network. *International Federation of Digital Seismograph Networks*. https://doi.org/10.7914/SN/AK

Alaska Volcano Observatory-USGS. (1988). Alaska volcano observatory. *International Federation of Digital Seismograph Networks*. https://doi.org/10.7914/SN/AV

Alberta Geological Survey/Alberta Energy Regulator. (2013). Regional Alberta observatory for earthquake studies network. *International Federation of Digital Seismograph Networks*. https://doi.org/10.7914/SN/RV

Albuquerque Seismological Laboratory (ASL)/USGS. (1980). Us geological survey networks. *International Federation of Digital Seismograph Networks*. https://doi.org/10.7914/SN/GS

Albuquerque Seismological Laboratory (ASL)/USGS. (1990). United States national seismic network. *International Federation of Digital Seismograph Networks*. https://doi.org/10.7914/SN/US

Albuquerque Seismological Laboratory (ASL)/USGS. (1992). New China digital seismograph network. *International Federation of Digital Seismograph Networks*. https://doi.org/10.7914/SN/IC

Albuquerque Seismological Laboratory (ASL)/USGS. (1993). Global telemetered seismograph network (USAF/USGS). *International Federation of Digital Seismograph Networks*. https://doi.org/10.7914/SN/GT

Albuquerque Seismological Laboratory (ASL)/USGS. (1994). New England seismic network. *International Federation of Digital Seismograph Networks*. https://doi.org/10.7914/SN/NE

Albuquerque Seismological Laboratory (ASL)/USGS. (2006). Caribbean network. *International Federation of Digital Seismograph Networks*. https://doi.org/10.7914/SN/CU

Albuquerque Seismological Laboratory/USGS. (1988). Global seismograph network (GSN—IRIS/USGS). *International Federation of Digital Seismograph Networks*. https://doi.org/10.7914/SN/IU

Albuquerque Seismological Laboratory/USGS. (2013). Central and eastern US network. *International Federation of Digital Seismograph Networks*. https://doi.org/10.7914/SN/N4

Amanda Bustin. (2019). UBCISM. *International Federation of Digital Seismograph Networks*. https://doi.org/10.7914/SN/YP_2019

Andy Nyblade. (2019). Shale hills critical zone observatory mini-array experiment. *International Federation of Digital Seismograph Networks*. https://doi.org/10.7914/SN/XZ_2019

Meltzer, A., Beck, S., & Stachnik, J. (2021). High resolution imaging of the Pedernales earthquake rupture zone—Broadbands. *International Federation of Digital Seismograph Networks*. https://doi.org/10.7914/SN/XF_2021

Anthony, Q. (2001). Spokane WA earthquake swarm. *International Federation of Digital Seismograph Networks*. https://doi.org/10.7914/SN/XZ_2001

Reading, A., & Rawlinson, N. (2011). Bass strait. *International Federation of Digital Seismograph Networks*. https://doi.org/10.7914/SN/1P_2011

Arizona Geological Survey. (2007). Arizona broadband seismic network. *International Federation of Digital Seismograph Networks*. https://doi.org/10.7914/SN/AE

Brian Kennett. (1997). KIMBA97. *International Federation of Digital Seismograph Networks*. https://doi.org/10.7914/SN/7D_1997

Bureau of Economic Geology, The University of Texas at Austin. (2016). Texas seismological network. *International Federation of Digital Seismograph Networks*. https://doi.org/10.7914/SN/TX

California Institute of Technology and United States Geological Survey Pasadena. (1926). Southern California seismic network. *International Federation of Digital Seismograph Networks*. https://doi.org/10.7914/SN/CI

Chamberlain, C. (2022). Puysegur tremor and nucleation geophysical observatory. *International Federation of Digital Seismograph Networks*. https://doi.org/10.7914/SN/7D_2022

Cascades Volcano Observatory/USGS. (2001). Cascade chain volcano monitoring. *International Federation of Digital Seismograph Networks*. https://doi.org/10.7914/SN/CC

Chris, H. (2014). Idaho Teton dam. *International Federation of Digital Seismograph Networks*. https://doi.org/10.7914/SN/XZ_2014

Larsen, C., & West, M. (2009). Collaborative research: Relating glacier-generated seismicity to ice motion, basal processes and iceberg calving. *International Federation of Digital Seismograph Networks*. https://doi.org/10.7914/SN/XF_2009

Christian Poppeliers. (2015). Measuring ambient noise of ocean breakers. *International Federation of Digital Seismograph Networks*. https://doi.org/10.7914/SN/XZ_2015

Johnson, C. W., Vernon, F., Ben-Zion, Y., & Nakata, N. (2018). Sage brush flats seismic experiment on interaction of wind with ground motion. *International Federation of Digital Seismograph Networks*. https://doi.org/10.7914/SN/7A_2018

Cornou, C., Bard, P.-Y., & RESIF. (2014). Seismic network YP: French part of the Argostoli (Greece) aftershock experiment (Resif-Sismob). *RESIF—Réseau Sismologique et géodésique Français*. https://doi.org/10.15778/RESIF.YP2014

Costanzo, A., Falcone, S., La Piana, C., Caserta, A., Doumaz, F., Buongiorno, M. F., et al. (2022). *Urban seismic network (RUSN-CAL-INGV)—Real time urban seismic network managed by CALabrian headquarters of INGV for monitoring urban areas, critical infrastructures and cultural heritage sites*. Istituto Nazionale di Geofisica e Vulcanologia (INGV). https://doi.org/10.13127/SD/O5NRHMP9N7

Dahm, T., Isken, M. P., Milkereit, C., Mikulla, S., Yuan, X., Sens-Schönfelder, C., et al. (2023). Eifel Large-n Seismic Network (ELSN). *GFZ Data Services*. https://doi.org/10.14470/1R080930

Dan, K. (2008). MROI vibration studies. *International Federation of Digital Seismograph Networks*. https://doi.org/10.7914/SN/Z7_2008

Department of Meteorology and Hydrology—National Earthquake Data Center. (2016). Myanmar national seismic network. *International Federation of Digital Seismograph Networks*. https://doi.org/10.7914/SN/MM

Schutt, D., & Aster, R. (2015). The Mackenzie Mountains transect: Active deformation from margin to craton. *International Federation of Digital Seismograph Networks*. https://doi.org/10.7914/SN/7C_2015

Dietrich, L., & Moreno, M. (2023). So297-land: Onshore extension of the 2023 rv so297 eperiment between Copiapó and Taltal, Chile. *International Federation of Digital Seismograph Networks*. https://doi.org/10.7914/KHGA-FW51

Doubre, C., Leroy, S., Keir, D., Pagli, C., & RESIF. (2021). Study of the structure of the lithosphere from the continental plateau of western Ethiopia to the active afar rift (Resif-Sismob). *RESIF—Réseau Sismologique et géodésique Français*. https://doi.org/10.15778/RESIF.YP2017

Douglas, W. (2012). Mantle serpentinization and water cycling through the Mariana trench and forearc. *International Federation of Digital Seismograph Networks*. https://doi.org/10.7914/SN/XF_2012

Douglas, W., & Maria Beatrice Magnani. (2018). Solid earth response of the Patagonia Andes to post-little ice age glacial retreat. *International Federation of Digital Seismograph Networks*. https://doi.org/10.7914/SN/1P_2018

Seylabi, E., Tyler, S., Hatch, R., & Saltiel, S. (2021). Sub-surface imaging of the west Reno basin. *International Federation of Digital Seismograph Networks*. https://doi.org/10.7914/SN/6E_2021

Kruger, F., Rietbrock, A., Rychert, C., Harmon, N., & Collier, J. (2016). Volatile recycling at the lesser Antilles arc: Processes and consequences. *International Federation of Digital Seismograph Networks*. https://doi.org/10.7914/SN/XZ_2016

Frank, V. (1982). Anza regional network. *International Federation of Digital Seismograph Networks*. https://doi.org/10.7914/SN/AZ

Frank, V. (2014). Piñon flats observatory array. *International Federation of Digital Seismograph Networks*. https://doi.org/10.7914/SN/PY

Vernon, F., & Jon Fletcher. (1987). Anza borehole experiment. *International Federation of Digital Seismograph Networks*. https://doi.org/10.7914/SN/XF_1987

Vernon, F., & Dueker, K. (2000). Laramie telemetered broad-band array. *International Federation of Digital Seismograph Networks*. https://doi.org/10.7914/SN/XF_2000

Geoscience Australia. (2021). *Australian national seismograph network data collection*. Commonwealth of Australia. (Geoscience Australia). https://doi.org/10.26186/144675

GEUS Geological Survey of Denmark and Greenland. (1976). Danish seismological network. *International Federation of Digital Seismograph Networks*. https://doi.org/10.7914/NW3X-DF02

Gordon, H. (2016). Flow and fracture dynamics in an ice shelf lateral margin: Observations and modeling of the Mcmurdo shear zone. *International Federation of Digital Seismograph Networks*. https://doi.org/10.7914/SN/YP_2016

Haberland, C., Ryberg, T., & Kirsch, M. (2021). The Geyer seismic network. *GFZ Data Services*. https://doi.org/10.14470/KS7575632014

Joughin, I., Das, S., & Behn, M. (2006). Behavior of supraglacial Lakes and their role in outlet glacier dynamics and mass balance of the Greenland ice sheet. *International Federation of Digital Seismograph Networks*. https://doi.org/10.7914/SN/Y6_2006

Institut De Physique Du Globe De Paris (IPGP). (2008). *GNSS, seismic broadband and strong motion permanent networks in west Indies*. Institut de physique du globe de Paris (IPGP). https://doi.org/10.18715/ANTILLES.WI

Institut de physique du globe de Paris (IPGP), and École et Observatoire des Sciences de la Terre de Strasbourg (EOST). (1982). *Geoscope, French global network of broad band seismic stations*. Institut de physique du globe de Paris (IPGP). https://doi.org/10.18715/GEOSCOPE.G

Institute of Earth Sciences, Academia Sinica, Taiwan. (1996). Broadband array in Taiwan for seismology. *International Federation of Digital Seismograph Networks*. https://doi.org/10.7914/SN/TW

Institute of Geophysics China Earthquake Administration (IGPCEA). (2000). China national seismic network, data management centre of China national seismic network at institute of geophysics, CEA. *International Federation of Digital Seismograph Networks*. https://doi.org/10.7914/SN/CB

Instituto Nicaraguense de Estudios Territoriales (INETER). (1975). Nicaraguan seismic network. *International Federation of Digital Seismograph Networks*. https://doi.org/10.7914/SN/NU

IRIS HQ (DC). (2012). Greenland ice sheet monitoring network. *International Federation of Digital Seismograph Networks*. https://doi.org/10.7914/SN/GG

Iris, OBSIP. (2011). Cascadia initiative community experiment—OBS component. *International Federation of Digital Seismograph Networks*. https://doi.org/10.7914/SN/7D_2011

IRIS Transportable Array. (2003). Usarray transportable array. *International Federation of Digital Seismograph Networks*. https://doi.org/10.7914/SN/TA

Istituto Nazionale di Oceanografia e di Geofisica Sperimentale. (1992). Antarctic seismographic Argentinean Italian network—Asain. *International Federation of Digital Seismograph Networks*. https://doi.org/10.7914/SN/AI

James Conder. (2013). Wabash valley seismic zone. *International Federation of Digital Seismograph Networks*. https://doi.org/10.7914/SN/6E_2013

Farrell, J., Koper, K., & Sohn, R. (2018). Yellowstone Lake microseism 2018. *International Federation of Digital Seismograph Networks*. https://doi.org/10.7914/SN/Y6_2018

John, L. (2018). Surface-wave characterization of the shoal nuclear blast cavity and rubble chimney. *International Federation of Digital Seismograph Networks*. https://doi.org/10.7914/SN/6E_2018

Louie, J., & Breitmeyer, R. (2019). Community, arts, and environmental setting of fly geyser, Nevada. *International Federation of Digital Seismograph Networks*. https://doi.org/10.7914/SN/Y6_2019

John, N. (2002). Collaborative research: Lithospheric scale dynamics of active Mountain building along the Himalayan-Tibetan collision zone. *International Federation of Digital Seismograph Networks*. https://doi.org/10.7914/SN/XF_2002

Keir, K., & Ayele. (2016). Rift valley volcanism past present and future. *International Federation of Digital Seismograph Networks*. https://doi.org/10.7914/SN/Y6_2016

KNMI. (2006). *Caribbean Netherlands seismic network*. Royal Netherlands Meteorological Institute (KNMI). https://doi.org/10.21944/DFFA7A3F-7E3A-3B33-A436-516A01B6AF3F

Lamont Doherty Earth Observatory (LDEO), Columbia University. (1970). Lamont-Doherty cooperative seismographic network. *International Federation of Digital Seismograph Networks*. https://doi.org/10.7914/SN/LD

Rocha, M. (2021). Carajás mineral province seismic network. *International Federation of Digital Seismograph Networks*. https://doi.org/10.7914/SN/7A_2021

Long, M., & Paul, W. (2013). Mid-Atlantic geophysical integrative collaboration. *International Federation of Digital Seismograph Networks*. https://doi.org/10.7914/SN/7A_2013

Meredith, N. (2014). Understanding Precambrian to present assembly of Greenland. *International Federation of Digital Seismograph Networks*. https://doi.org/10.7914/SN/XF_2014

Salmon, M., Balfour, N., Sambridge, M., Mousavi, S., & Pickle, R. (2011). Australian seismometers in schools. *AusPass*. https://doi.org/10.7914/SN/S1

Natural Resources Canada. (1975). Canadian national seismograph network. *Natural Resources Canada*. https://doi.org/10.7914/SN/CN

Harbison, N., & Craig, O. 'N. (2024). Georgetown seismic traverse, north Queensland. *International Federation of Digital Seismograph Networks*. https://doi.org/10.7914/3V05-SW22

New Mexico Tech. (1999). New Mexico tech seismic network. *International Federation of Digital Seismograph Networks*. https://doi.org/10.7914/0ABK-1345

Nicholas, S. (2017). Geodes San Francisco volcanic field active seismic experiment 2017. *International Federation of Digital Seismograph Networks*. https://doi.org/10.7914/TYZX-JN40

NOAA National Oceanic and Atmospheric Administration (USA). (1967). National tsunami warning center Alaska seismic network. *International Federation of Digital Seismograph Networks*. https://doi.org/10.7914/SN/AT

Finnegan, N., & Schwartz, S. (2023). Nodal seismometer deployment at oak ridge earthflow near San Jose, CA. *International Federation of Digital Seismograph Networks*. https://doi.org/10.7914/PNFW-J315

Northern California Earthquake Data Center. (2014). *Berkeley digital seismic network (BDSN)*. Northern California Earthquake Data Center. https://doi.org/10.7932/BDSN

NSF Ocean Observatories Initiative. (2013). Ocean observatories initiative. *International Federation of Digital Seismograph Networks*. https://doi.org/10.7914/SN/OO

Paul, A., Mordret, A., Aubert, C., Chevrot, S., Sylvander, M., & Pauchet, H., & RESIF. (2024). MACIV-profiles temporary experiment of seismic imaging of the lithospheric structure of the French Massif Central along 3 profiles to complete the MACIV-BB broadband network to be deployed in 2024, France (Resif-Sismob). *RESIF—Réseau Sismologique et géodésique Français*. https://doi.org/10.15778/RESIF.XF2024

Bedrosian, P., Morris, J. R., Goldman, M., & Bloss, B. R. (2017). Kansas and Nebraska magnetotelluric time series (USGS-GGGSC, Kansas 2017 long period). *International Federation of Digital Seismograph Networks*. https://doi.org/10.7914/SN/Z7_2017

Penn State University. (2004). Pennsylvania state seismic network. *International Federation of Digital Seismograph Networks*. https://doi.org/10.7914/SN/PE

Share, P.-E., & Frank, V. (2019). Dense nodal deployment at some test sites for the upcoming Faultscan project. *International Federation of Digital Seismograph Networks*. https://doi.org/10.7914/SN/6E_2019

Pilz, M., Ohrnberger, M., & Roux, P. (2023). Meta-wt. *GFZ Data Services*. https://doi.org/10.14470/KS178126

Ramon Carbonell. (2012). Wide-angle seismic reflection experiment across the central Iberian zone; Iberia Peninsula. *International Federation of Digital Seismograph Networks*. https://doi.org/10.7914/SN/7A_2012

Regional Integrated Multi-Hazard Early Warning System (RIMES Thailand). (2008). Regional integrated multi-hazard early warning system. *International Federation of Digital Seismograph Networks*. https://doi.org/10.7914/SN/RM

Aster, R., & Kyle, P. (1999). Mount Erebus seismic studies. *International Federation of Digital Seismograph Networks*. https://doi.org/10.7914/SN/XZ_1999

Ritter, J. R. R., Schmidt, B., Haberland, C., & Weber, M. (2014). Deep-tee phase 1. *GFZ Data Services*. https://doi.org/10.14470/6C709520

White, R. (2010). Northern volcanic zone. *International Federation of Digital Seismograph Networks*. https://doi.org/10.7914/SN/Z7_2010

Hansen, R., & Gary, P. (2005). Collaborative research: St. Elias erosion/tectonics project. *International Federation of Digital Seismograph Networks*. https://doi.org/10.7914/SN/XZ_2005

Rufus Catchings. (2014). 2014 NAPA earthquake response. *International Federation of Digital Seismograph Networks*. https://doi.org/10.7914/SN/7C_2014

Ryberg, T., & Haberland, C. (2008). Lake Toba seismic network, Sumatra, Indonesia. *GFZ Data Services*. https://doi.org/10.14470/2N934755

De Angelis, S., & Diaz-Moreno, A. (2017). INFRA-ETNA. *International Federation of Digital Seismograph Networks*. https://doi.org/10.7914/SN/XF_2017

Mader, S., Neuffer, T., & Busch, S. (2022). DB MISS. *International Federation of Digital Seismograph Networks*. https://doi.org/10.7914/SN/1P_2022

Scripps Institution of Oceanography. (1986). Global seismograph network—IRIS/IDA. *International Federation of Digital Seismograph Networks*. https://doi.org/10.7914/SN/II

Servicio Geológico Colombiano. (1993). Red sismologica nacional de Colombia. *International Federation of Digital Seismograph Networks*. https://doi.org/10.7914/SN/CM

Servicio Sismológico Nacional, Instituto de Geofísica, Universidad Nacional Autónoma de México. (2017). *Mx. Servicio Sismológico Nacional, Instituto de Geofísica*. Universidad Nacional Autónoma de México. https://doi.org/10.21766/ssnmx/sn/mx

De Angelis, S. (2018). Experiment in Fuego. *International Federation of Digital Seismograph Networks*. https://doi.org/10.7914/SN/XZ_2018

Socquet, A., Baez, J. C., Moreno, M., & Langlais, M., & DEEP-Trigger Team, Geophysics Technical Service At ISTerre, and RESIF. (2020). Deep_trigger temporary experiment in the subduction zone Peru/Chile, Chile (Resif-Sismob). *RESIF—Réseau Sismologique et géodésique Français*. https://doi.org/10.15778/RESIF.XZ2020

Sridhar, A. (1995). Antarctic microearthquake project, monitoring of ice stream C, west Antarctica. *International Federation of Digital Seismograph Networks*. https://doi.org/10.7914/SN/XF_1995

Day, S., & Vernon, F. (1994). Peninsular range. *International Federation of Digital Seismograph Networks*. https://doi.org/10.7914/SN/XF_1994

Grand, S., & Ni, J. (2006). Mapping the Rivera subduction zone. *International Federation of Digital Seismograph Networks*. https://doi.org/10.7914/SN/XF_2006

Grand, S., & Ni, J. (2009). Collaborative research: Northeast China extended seismic array: Deep subduction, mantle dynamics and lithospheric evolution beneath northeast China. *International Federation of Digital Seismograph Networks*. https://doi.org/10.7914/SN/YP_2009

Susan Bilek. (2024). Bedload monitoring—Flume test. *International Federation of Digital Seismograph Networks*. https://doi.org/10.7914/Y85B-6956

Leroy, S. (2003). DHOFAR seismic experiment. *International Federation of Digital Seismograph Networks*. https://doi.org/10.7914/SN/XZ_2003

Tiberi, C., & Gautier, S., & RESIF. (2020). Hazard in Tanzanian rift: Hatari (Resif-Sismob). *RESIF—Réseau Sismologique et géodésique Français*. https://doi.org/10.15778/RESIF.XF2018

Tilmann, F., Heit, B., Moreno, M., & González-Vidal, D. (2021). Anillo. *GFZ Data Services*. https://doi.org/10.14470/L17575324477

Tulane University, Louisiana State University, and University Louisiana Lafayette. (2019). Induced seismicity in Louisiana. *International Federation of Digital Seismograph Networks*. https://doi.org/10.7914/SN/Z7_2019

Universidad de Chile. (2012). Red sismologica nacional. *International Federation of Digital Seismograph Networks*. https://doi.org/10.7914/SN/C1

University of Nevada, Reno. (1971). Nevada seismic network. *International Federation of Digital Seismograph Networks*. https://doi.org/10.7914/SN/NN

University of Oregon. (1990). Pacific northwest seismic network—University of oregon. *International Federation of Digital Seismograph Networks*. https://doi.org/10.7914/SN/UO

University of Puerto Rico. (1986). Puerto Rico seismic network and Puerto Rico strong motion program. *International Federation of Digital Seismograph Networks*. https://doi.org/10.7914/SN/PR

University of Washington. (1963). Pacific northwest seismic network—University of Washington. *International Federation of Digital Seismograph Networks*. https://doi.org/10.7914/SN/UW

USGS Alaska Anchorage. (2000). Usgs Northern Mariana Islands network. *International Federation of Digital Seismograph Networks*. https://doi.org/10.7914/SN/MI

Utrecht University (UU Netherlands). (1983). NARS. *International Federation of Digital Seismograph Networks*. https://doi.org/10.7914/SN/NR

Various, I. (1965). International miscellaneous stations. *International Federation of Digital Seismograph Networks*. https://doi.org/10.7914/VEFQ-VH75

Vergne, J., Doubre, C., & Leroy, S. (2014). Seismic network 7c: Dora experiment (Resif-Sismob). *RESIF—Réseau Sismologique et géodésique Français*. https://doi.org/10.15778/RESIF.7C2009

Vergne, J., & RESIF. (2021). Rittershoffen (Bas-Rhin, France) dense nodal seismic array temporary experiment (Resif-Sismob). *RESIF—Réseau Sismologique et géodésique Français*. https://doi.org/10.15778/RESIF.Z72018

Shen, W. (2023). Career: A comprehensive seismic investigation to the crust and uppermost mantle beneath the south pole, east Antarctica. *International Federation of Digital Seismograph Networks*. https://doi.org/10.7914/TVW3-C709

Fan, W., Huang, Y., & Shawn Wei, S. (2018). Lake-induced earthquakes in Lake Erie. *International Federation of Digital Seismograph Networks*. https://doi.org/10.7914/SN/7D_2018

Thelen, W., & Paul, B. (2009). Yakima landslide ramp. *International Federation of Digital Seismograph Networks*. https://doi.org/10.7914/SN/7D_2009

Yuan, X., Schurr, B., Haberland, C., Abdybachaev, U., & Sharshebaev, A. (2019). Multi-scale imaging of the main Pamir thrust faults within the framework of catena project—Climatic and tectonic natural hazards in central Asia. *GFZ Data Services*. https://doi.org/10.14470/2N7564774946

Zhao, L., Paul, A., & Solarino, S., & RESIF. (2016). Seismic network YP: Cifalps temporary experiment (China-Italy-France Alps seismic transect). *RESIF—Réseau Sismologique et géodésique Français*. https://doi.org/10.15778/RESIF.YP2012